Journal of Magnetic Resonance 352 (2023) 107459

Contents lists available at ScienceDirect

Journal of Magnetic Resonance

journal homepage: www.elsevier.com/locate/jmr

# Comparison of methods for $^{14}$N-$^{1}$H recoupling in $^{14}$N-$^{1}$H HMQC MAS NMR

Ben P. Tatman [a,b], Haritosh Modha [a], Steven P. Brown [a,*]

[a] Department of Physics, University of Warwick, Coventry CV4 7AL, UK
[b] Department of Chemistry, University of Warwick, Coventry CV4 7AL, UK

ARTICLE INFO

*Article history:*
Received 31 January 2023
Revised 8 April 2023
Accepted 19 April 2023
Available online 24 April 2023

*Keywords:*
NMR
MAS
Recoupling
Dipolar coupling
$^{14}$N
$^{1}$H
TRAPDOR
Rotary resonance recoupling

ABSTRACT

$^{1}$H-detected $^{14}$N heteronuclear multiple-quantum coherence (HMQC) magic-angle-spinning (MAS) NMR experiments performed at fast magic-angle spinning (≥50 kHz) are finding increasing application, e.g., to pharmaceuticals. Of importance to the efficacy of these techniques is the recoupling technique applied to reintroduce the $^{1}$H-$^{14}$N dipolar coupling. In this paper, we compare, by experiment and 2-spin density matrix simulations, two classes of recoupling scheme: first, those based on $n$ = 2 rotary resonance, namely R$^3$ and spin-polarisation inversion SPI-R$^3$, and the symmetry based SR4$_1^2$ method and, second, the TRAPDOR method. Both classes require optimisation depending on the magnitude of the quadrupolar interaction, and thus there is a compromise choice for samples with more than one nitrogen site, as is the case for the studied dipeptide β-AspAla that contains two nitrogen sites with a small and large quadrupolar coupling constant. Considering this, we observe better sensitivity for the TRAPDOR method, though noting the marked sensitivity of TRAPDOR to the $^{14}$N transmitter offset, with both SPI-R$^3$ and SR4$_1^2$ giving similar recoupling performance.



## 1. Introduction

Nitrogen is a ubiquitous element in a range of biological and pharmacological systems. Unfortunately, the application of solid-state NMR to such systems is limited by the difficulties in observing either of the stable isotopes of nitrogen. Nitrogen-14, while highly abundant (99.63%), is a low-gamma spin-1 nucleus with typically significant quadrupolar couplings on the order of MHz. The spin-1/2 isotope, nitrogen-15, is limited by its very low natural abundance.

It has been found that the use of indirect $^{14}$N detection *via* abundant spy nuclei, combined with magic-angle spinning (MAS) can help to avoid the issues associated with $^{14}$N [1,2]. Employing fast MAS at frequencies in excess of 50 kHz to ensure sufficiently long coherence lifetimes and to reduce line broadening, $^{1}$H detection has been found to be advantageous [3,4]. Such experiments with indirect detection of $^{14}$N *via* $^{1}$H have found use in the study of a range of samples including supramolecular self-assembly, co-crystals, and amorphous dispersions of pharmaceuticals [5–21].

The majority of studies using this indirect detection method have made use of heteronuclear $^{14}$N-$^{1}$H multiple quantum coherence (HMQC) [3,4] experiments, in which correlation is obtained by recoupling of the $^{14}$N-$^{1}$H dipolar coupling. Note that the specified order of nuclei in this paper corresponds to the evolution of $^{14}$N single-quantum coherence (as part of the HMQC) in, first, $t_1$, and, second, $^{1}$H magnetisation in $t_2$. $^{14}$N-$^{1}$H cross polarisation (CP) based techniques have also been presented [19,20]. The efficiency of recoupling of the $^{14}$N-$^{1}$H heteronuclear dipolar coupling is of key importance to these techniques. The majority of these HMQC based correlation experiments have relied upon $n$ = 2 rotary resonance recoupling, R$^3$ [2,3,22,23], as also implemented in the spin-polarisation inversion SPI-R$^3$ [5,14,24,25] and symmetry-based SR4$_1^2$ [4,26] techniques. Such experiments require $^{14}$N pulses whose optimisation is dependent on the $^{14}$N quadrupolar environment, and are referred to here as D-HMQC. Alternatively, the TRAnsfer of Population in DOuble Resonance (TRAPDOR) [27–29] approach has been recently shown to be a promising $^{14}$N-$^{1}$H recoupling technique in the T-HMQC experiment [7,30]. The optimization of TRAPDOR recoupling, and specifically the $^{14}$N transmitter offset is, however, strongly dependent on the quadrupolar environment of the sites of interest [30–32]. Pulse sequences for the rotary resonance recoupling/symmetry-based and TRAPDOR-based $^{14}$N-$^{1}$H HMQC MAS NMR experiments are shown in Fig. 1.

In this paper, we provide an overview of prior studies using $^{14}$N-$^{1}$H HMQC techniques, specifically with regards to the recoupling technique used. Following this, we compare the

* Corresponding author.
*E-mail address:* S.P.Brown@warwick.ac.uk (S.P. Brown).

https://doi.org/10.1016/j.jmr.2023.107459
1090-7807/

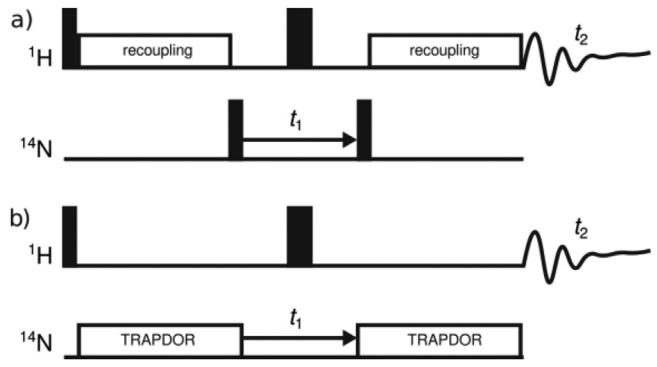


**Fig. 1.** Pulse sequences for $^{14}$N-$^1$H HMQC MAS NMR experiments: a) D-HMQC with $^1$H recoupling, b) T-HMQC with TRAPDOR recoupling applied to $^{14}$N. Thin and thick black rectangles on the $^1$H channel indicate 90° and 180° pulses, respectively. Black rectangles on $^{14}$N indicate RF pulses which are used to convert between $S_z$ and $S_{x,y}$ within a heteronuclear coherence state.

rotary-resonance-recoupling based schemes and the use of TRAPDOR recoupling via both experiment and 2-spin density matrix simulations for the dipeptide β-AspAla that contains two nitrogen sites with a small and large quadrupolar coupling constant.

## 2. Methods

### 2.1. Solid-State NMR

Our test system is the β-aspartyl L-alanine dipeptide (β-AspAla), which possesses two nitrogen sites with a small and a large quadrupolar coupling constant. This was purchased from Bachem (Bubendorf, Switzerland) and packed as received into a 1.3 mm zirconia rotor. 2D $^{14}$N-$^1$H HMQC experiments were performed on a Bruker Avance III spectrometer operating at a $^1$H and $^{14}$N Larmor frequency of 500.1 MHz and 36.2 MHz, respectively. A 1.3 mm HXY probe in double resonance mode was used. For 90° and 180° pulses, a $^1$H nutation frequency of 100 kHz was used, corresponding to a $^1$H 90° and 180° pulse duration of 2.5 μs and 5 μs, respectively. RF pulses on $^{14}$N were applied using a nutation frequency of 45 kHz for 9 μs, as calibrated using solid $NH_4Cl$. In all experiments, the $^1$H transmitter was placed at 6.0 ppm, and the $^{14}$N transmitter at −3.0 ppm. A recycle delay of 2 s was used. For 2D experiments, States-TPPI was used to achieve sign discrimination in the indirect dimension. For 2D $^{14}$N-$^1$H HMQC experiments, 16 transients were coadded for 96 (60 kHz MAS) or 48 (50 kHz MAS) rotor-synchronized $t_1$ increments (16.7 μs at 60 kHz, 20 μs at 50 kHz), corresponding to a total experimental time of 52 min and 26 min, respectively.

For D-HMQC experiments, the phase cycle used was $^1$H 90° {y − y}, $^1$H 180° {x}, first $^{14}$N pulse {4(x) 4(−x)}, second $^{14}$N pulse {2(x) 2(−x)}, detection {x − x − x x − x x x − x}. For T-HMQC experiments, the phase cycle was as follows: $^1$H 90° {8(+x) 8 (−x)}, $^1$H 180° {x x y y − x − x − y − y}, first $^{14}$N TRAPDOR period {x − x}, second $^{14}$N TRAPDOR period {x}, detection {x − x − x x x − x − x x − x x x − x − x x x − x}.

$^1$H chemical shifts were referenced to tetramethylsilane (TMS) using previously known chemical shifts of β-aspartyl L-alanine [33]. $^{14}$N shifts were referenced using solid $NH_4Cl$ at a shift of −341.2 ppm, corresponding to liquid $CH_3NO_2$ at 0 ppm [34]. To convert to be equivalent with the frequently used $^{15}$N chemical shift scale used in protein NMR where the alternative IUPAC reference (see Appendix 1 of ref [35]) is liquid $NH_3$, it is necessary to add 379.5 ppm to the given values [36].

### 2.2. GIPAW calculation

Density functional theory (DFT) calculations were performed using CASTEP 20.11 [37]. First, a geometry optimisation of all atom positions and the unit cell parameters starting from the single-crystal X-ray diffraction structure of β-aspartyl L-alanine (CCDC: FUMTEM) was performed [38]. Upon geometry optimisation, the unit cell dimensions changed from $a$ = 4.845 Å, $b$ = 9.409 Å, and $c$ = 19.170 Å to $a$ = 4.946 Å, $b$ = 9.794 Å, and $c$ = 20.870 Å, with $\alpha$ = 90°, $\beta$ = 90°, and $\gamma$ = 90°. The Perdew Burke Ernzerhof (PBE) exchange correlation functional [39], was used with a plane-wave basis set with ultrasoft pseudopotentials and a cut-off energy of 700 eV. A minimum Monkhorst-Pack grid spacing of $2\pi \times 0.1$ Å$^{-1}$ was used. The GIPAW method [40,41] was used to calculate the NMR parameters.

### 2.3. Density-Matrix simulations

Two-spin simulations were carried out using SIMPSON 4.2.1 [42–44] using a REPULSION [45] set of 66 crystallite orientations and 19 gamma angles (see representative input files in section S2 of the Supporting Information). To match the experimental NMR data, simulations were performed for a $^1$H Larmor frequency of 500 MHz and a MAS frequency of 50 or 60 kHz. Simulations were performed for spin-system parameters corresponding to those from the GIPAW calculation (see section 2.2), as generated using Magresview [46]. Specifically, for the NH site, $C_Q$ = 3.35 MHz, $\eta_Q$ = 0.41, $\delta_{iso}$ = −245.0 ppm and for the $NH_3^+$ site, $C_Q$ = 1.24 MHz, $\eta_Q$ = 0.25, $\delta_{iso}$ = −348.5 ppm. Note that the calculated chemical shift tensors (both isotropic and anisotropic chemical shift were included, as well as the Euler angles for the relative orientation of the principal axes systems of the anisotropic interactions) were determined from the calculated chemical shielding tensors according to $(\partial^{calc}) = \sigma_{ref} - \sigma_{calc}$, where reference shieldings of 30.5 ppm and −160 ppm were used for $^1$H and $^{14}$N, respectively.

For the NH and $NH_3^+$ groups, the N–H distances from the DFT geometry-optimised structure are 1.03 Å and 1.04 Å, respectively. Dipolar couplings (in Hz) were calculated using the following equation:

$$D_{NH} = -\left(\frac{\mu_0}{4\pi}\right)\left(\frac{\gamma_H \gamma_N \hbar}{2\pi}\right)\langle r_{i,j}^{-3}\rangle, \quad (1)$$

where $\gamma_H$ and $\gamma_N$ are the gyromagnetic ratios for $^1$H and $^{14}$N, respectively, $r$ is the internuclear distance, $\hbar$ is the reduced Planck's constant, and $\mu_0$ is the vacuum permeability. Using Eq. (1), $D_{NH}$ is equal to 8.0 kHz for the NH group. For the $NH_3^+$ group, a $D_{NH}$ = 3.9 kHz was used, corresponding a nominal scaling of 0.5 to take into account the $NH_3^+$ group rotation, according to $P_2(\cos(\theta))$ $(= \frac{1}{2}(3cos^2(\theta) - 1))$, where $\theta$ is the angle between the N–H internuclear vector and the three-site jump axis [47].

## 3. Results

### 3.1. β-aspartyl L-alanine as a model system

Here, we make use of experiment and simulation to compare these techniques as applied to β-aspartyl L-alanine (β-Asp Ala), a dipeptide possessing two nitrogen environments, namely a NH and a $NH_3^+$ group, with significantly different quadrupolar environments (see Table 1 and Fig. 2). As different aspects of the $^{14}$N-$^1$H HMQC experiment are sensitive to this quadrupolar environment, β-Asp Ala is a useful compound to evaluate optimisation for the case of the presence of sites with varying quadrupolar interaction.

The quadrupolar product, $P_Q$, is given as

**Table 1**
The $^{14}N$ quadrupolar parameters and chemical shifts for the nitrogen sites in β-AspAla, calculated using the GIPAW method (see section 2.2) and a comparison of calculated and experimental $^{14}N$ shifts.

| Nitrogen Site | $C_Q$/MHz | $\eta_Q$ | $P_Q$/MHz | $\delta^Q_{iso}/ppm$[a] | $\delta_{iso}/ppm$ | $\delta_{calc}/ppm$ | $\delta_{expt}/ppm$ |
|---|---|---|---|---|---|---|---|
| $NH_3$ | 1.24 | 0.25 | 1.25 | 90.2 | −348.5 | −258.3 | −270 ± 10 |
| NH | 3.35 | 0.41 | 3.44 | 681.3 | −245.0 | 436.3 | 360 ± 10 |

[a] See Eq. (5), as calculated for a $^1H$ Larmor frequency of 500 MHz.

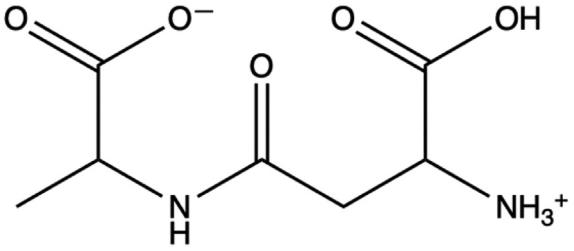


**Fig. 2.** The chemical structure of β-aspartyl L-alanine (β-AspAla).

$$P_Q = C_Q\sqrt{1+\left(\eta_Q^2/3\right)}, \tag{2}$$

where the quadrupolar coupling constant, $C_Q$, and the asymmetry parameter, $\eta_Q$, are related to the components of the quadrupolar coupling tensor in its principal axis system, with principal elements defined such that $|V_{33}| \geq |V_{22}| \geq |V_{11}|$, as:

$$C_Q = \frac{eQV_{33}}{h} \tag{3}$$

$$\eta_Q = \frac{V_{11}-V_{22}}{V_{33}}. \tag{4}$$

The isotropic second-order quadrupolar shift is calculated for the $I = 1$ $^{14}N$ nucleus as [14,48]:

$$\delta^Q_{iso} = +\frac{3}{40}\left(\frac{P_Q}{\upsilon_0}\right)^2 \times 10^6, \tag{5}$$

with the observed $^{14}N$ shift being the sum of this and the isotropic chemical shift, $\delta_{iso}$. Noting the inverse dependence on the Larmor frequency in Eq. (5), there is a much larger shift dispersion for $^{14}N$ as compared to $^{15}N$, especially at moderate magnetic field. For example, the $^{14}N$ shift has been shown to be sensitive to changes in hydrogen bonding associated with co-crystal formation [15].

A representative 2D $^{14}N$-$^1H$ D-HMQC MAS NMR spectrum of β-aspartyl L-alanine recorded using $SR4_1^2$ recoupling is shown in Fig. 3. A short recoupling time of 167 μs (10 $\tau_r$) was used such that two-dimensional peaks are only observed for directly bonded N–H connectivties, namely the $NH_3^+$ and the NH peaks at a $^{14}N$ shift of −270 and +360 ppm, respectively. The two nitrogen environments have similar $^1H$ chemical shifts [33,49]. The large dispersion in $^{14}N$ shift arises predominantly from the second order isotropic quadrupolar shift owing to the significant difference in quadrupolar coupling constant, with the observed $^{14}N$ shift being the sum of the isotropic chemical shift and the isotropic second-order quadrupolar shift [14]. In all subsequent figures, slices corresponding to NH and $NH_3^+$ were extracted by summing the rows from 666 ppm to 94 ppm and from −69 ppm to −524 ppm, respectively, as indicated by the double-headed arrows in Fig. 3.

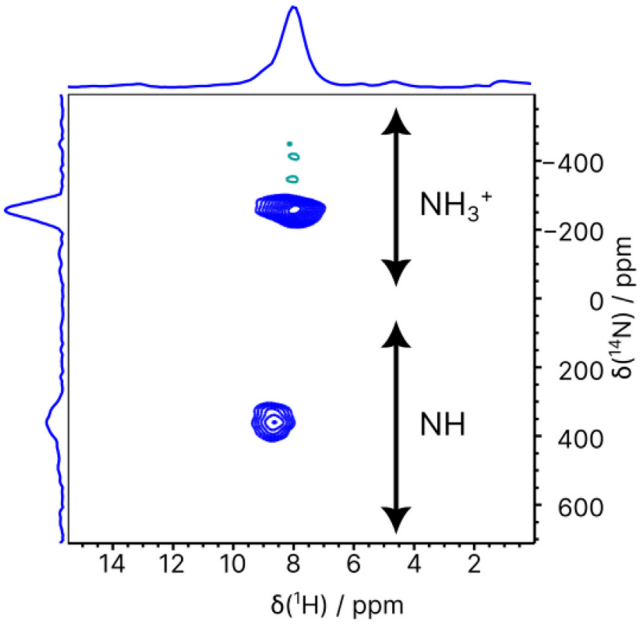


**Fig. 3.** A representative 2D $^{14}N$-$^1H$ D-HMQC MAS NMR spectrum with skyline projections of β-AspAla recorded at 60 kHz MAS and at a $^1H$ Larmor frequency of 500 MHz with 10 $\tau_r$ (167 μs) of $SR4_1^2$ recoupling at a $^1H$ nutation frequency of 120 kHz (the $n = 2$ condition). The base contour level is at 11.5% of the maximum peak height. Vertical double-headed arrows indicate the regions that are summed over for the intensities reported in the following figures.

### *3.2. $R^3$, SPI-$R^3$, and $SR4_1^2$ Recoupling: Introduction and review of applications*

Since the original introduction of the $^1H$-detected $^{14}N$ HMQC experiment [1,3], and its further application at 80 kHz MAS [4], a range of recoupling techniques have been utilised. The most common of these are based on rotary-resonance recoupling at the $n = 2$ condition ($R^3$) [2,3,22,50,51], notably spin-polarisation inversion $R^3$ (SPI-$R^3$) [5,24,25], and the symmetry-based $SR4_1^2$ [23,26]. More recently, double cross-polarisation (CP) [19,20] and TRAnsfer of Population in DOuble Resonance [27,29] (TRAPDOR) based techniques have been employed [7,30], and were recently compared for L-histidine·HCl·$H_2O$ by Hung et al. [30] Whilst $R^3$, SPI-$R^3$, and $SR4_1^2$ have all been compared directly in their application to the recoupling of correlations between spin-1/2 and half integer quadrupolar nuclei [24,52], $^{14}N$ presents the challenge both of being a spin-1 nucleus, and usually possesses a large quadrupolar coupling on the order of MHz. As such, reviewing these recoupling techniques is of key importance to this technique.

There are two primary families of recoupling sequence which we will consider in this paper. Rotary-resonance based recoupling techniques, such as $R^3$ or SPI-$R^3$, work by applying nutation frequencies which are at certain resonance conditions with respect to the MAS frequency [50,53]:

$$\nu_1 = n\nu_r. \tag{6}$$

By applying a nutation frequency equal to twice the spinning frequency it is possible to selectively recouple heteronuclear interactions. This is known as rotary-resonance recoupling at the $n = 2$ condition, here referred to simply as $R^3$. It has been found that by applying a phase inversion every rotor period, it is possible to obtain higher transfer efficiency and better offset dependence than for $R^3$, this is referred to here SPI-$R^3$ [5,14,24,25].

Symmetry-based recoupling is where specific symmetry relations between the spin and space states are utilised to selectively recouple particular symmetries of the NMR interactions. Such techniques have been reviewed previously [23]. $SR4_1^2$ is an example of a super-cycled symmetry sequence, where the base unit is $R4_1^2$, which selectively recouples heteronuclear interactions. This is followed by a phase inversion every rotor period (equivalent to that relating $R^3$ to SPI-$R^3$), and finally a $C3_6^1$ supercycle [26]. As stated above, all the rotary-resonance and symmetry-based recoupling techniques considered here require irradiation with a nutation frequency equal to twice the spinning frequency, $\nu_1 = 2\ \nu_R$. Fig. 4 shows an outline of how these different recoupling techniques are related to one another, and how they are built up out of their individual pulse elements.

These three recoupling sequences make up the majority of $^{14}$N-$^{1}$H HMQC experiments to date. The original applications of $^{14}$N-$^{1}$H HMQC to amino acids at 20 kHz and 30 kHz MAS made use of $R^3$ [3] and $R20_5^9$ [1,54] recoupling, respectively, though, with the later development of this technique at 80 kHz MAS, this has been superseded by $SR4_1^2$.[4] Following this, several studies have been published using either SPI-$R^3$ or $SR4_1^2$ recoupling to investigate different moderately sized organic molecules. For instance, Webber *et al.* made use of the $^{14}$N-$^{1}$H HMQC experiment with SPI-$R^3$ recoupling to study guanosine self-assembly [5]. Tatton et al. compared the application of SPI-$R^3$ at variable spinning frequencies (30, 45, 60 kHz) [14] and have presented applications to pharmaceuticals [6,55], co-crystals, and an amorphous dispersion at 60 kHz MAS [15]. SPI-$R^3$ has been further applied to probe intermolecular interactions in citrate salts [18], pyridinium fumarates [8,9], drug-polymer interactions [11], and amorphous dispersions [12].

The symmetry-based recoupling technique, $SR4_1^2$ has been used in a range of systems. Since its use in the first $^{1}$H-$^{14}$N HMQC experiment at 80 kHz MAS [4], it has been applied to the study of oligopeptides and polypeptides [21], pharmaceuticals [17], salts & cocrystals [13], tautomerism in azo-dyes [10], to measure distances in amino acids [56], and as part of an experiment to probe $^{14}$N-$^{14}$N correlations [16]. These applications are summarised in Table S1.

Despite the prevalence of these techniques, to the best of our knowledge, there has been no direct comparison of these $n = 2$ rotary-resonance recoupling techniques in their application to $^{14}$N-$^{1}$H correlation. As shown in Table S2, the different recoupling methods have been compared for heteronuclear correlation between spin $I = 1/2$, 3/2, and 5/2 nuclei.

### 3.3. $^{14}$N-$^{1}$H D-HMQC MAS NMR: Comparison of $R^3$, SPI-$R^3$, and $SR4_1^2$ recoupling for β-aspartyl L-alanine using experiment and density-matrix simulation

This section considers the dependence of recoupling efficiency for the $n = 2$ rotary resonance based recoupling techniques (see Fig. 4) on the nutation frequency and the recoupling duration. As these techniques rely on matching the nutation frequency to a precise resonance condition of the spinning frequency, this precise setting of this nutation frequency is of key importance. However, this is not achieved perfectly in experiment due to inhomogeneity of the $B_1$ field applied in a RF probe [57]. As such, a desirable characteristic of a recoupling sequence is how robust it is with respect to $B_1$ field inhomogeneity.

Fig. 5a shows an experimental comparison of the recoupled efficiency between the three techniques of interest, where the nominal $^{1}$H nutation frequency was varied from 100 to 92 kHz. $SR4_1^2$ (blue) shows the greatest robustness to mis-set of the nutation frequency, followed by SPI-$R^3$ for which roughly half the intensity is lost for a mis-set of 4 kHz. $R^3$ recoupling performs the worst, losing most of the signal with a small offset. This observation shows the importance of the phase inversion present in both SPI-$R^3$ and $SR4_1^2$, compensating for deviation of the nutation frequency from the $n = 2$ condition. In two-spin simulations (Fig. 5b), it appears that SPI-$R^3$ has higher robustness to mis-set of the nutation frequency. This difference compared to experiment may result due to the presence of other spins in the sample that are not considered in the 2-spin simulations and that may lead to increased dipolar dephasing if not explicitly recoupled. It is notable that, both in simulation and experiment, the NH site appears less affected by mis-set of the nutation frequency, though the NH intensity is significantly lower.

The recoupling time dependence is also of interest, as, at shorter recoupling times, it would be expected that only one-bond correlations would be observed. As shown in Fig. 6a, at longer recoupling times, peaks at other $^{1}$H chemical shifts due to longer-range proximities between the NH and the $NH_3^+$ nitrogen and other hydrogen atoms are observed [14]; in other systems, such correlations are valuable for identifying hydrogen bonding interactions [6,11,58]. For longer recoupling durations, there is more loss of signal due to decoherence in the spin-lock frame, and so an ideal sequence for viewing long-range correlations would show increased resilience to this. Comparing the three different recoupling sequences, both experimentally and with 2-spin simulations, Fig. 6 shows that $R^3$ suffers significantly from dephasing at long durations, with

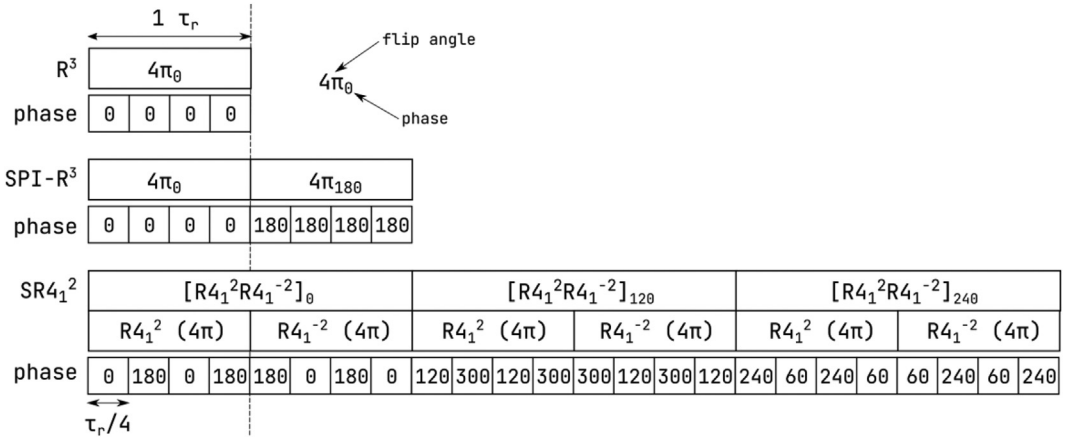


**Fig. 4.** Phase variation for the rotary-resonance and symmetry-based recoupling sequences considered here. In all cases, the applied nutation frequency is twice the spinning frequency, corresponding to the n = 2 $R^3$ condition.

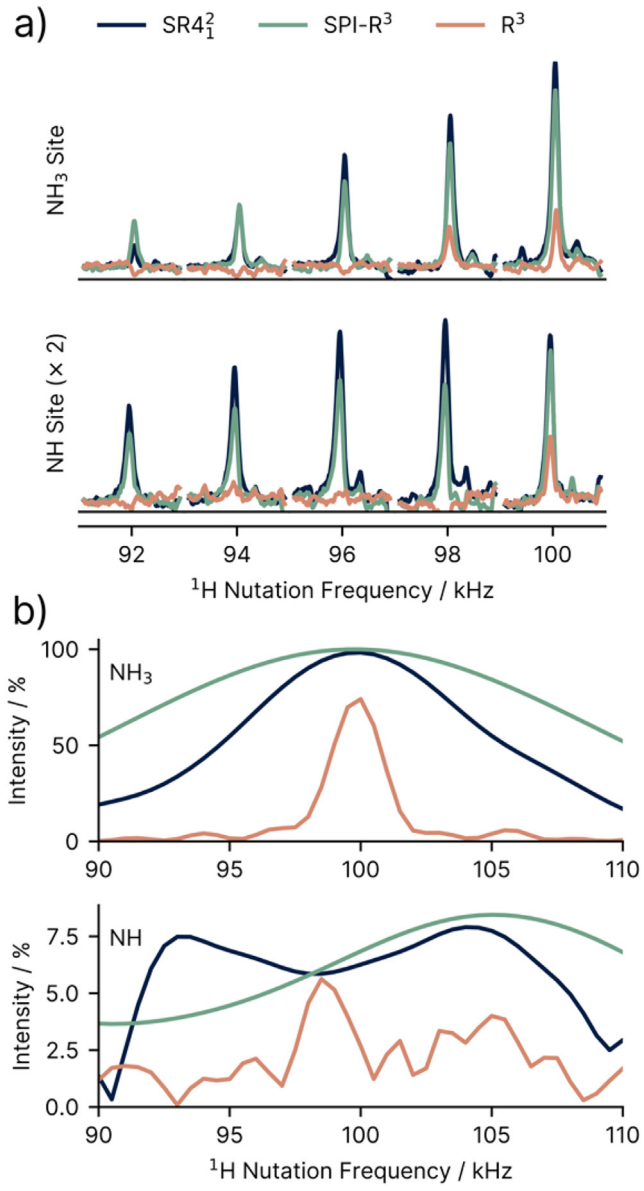


**Fig. 5.** Variation in $^{14}$N-$^1$H D-HMQC (see Fig. 1a) MAS NMR efficiency as a function of the $^1$H nutation frequency for each of the three $^1$H-channel recoupling techniques considered here, as applied to β-AspAla at 50 kHz MAS and at a $^1$H Larmor frequency of 500 MHz. a) Experimental spectra extracted by summing rows of 2D spectra over the sites of interest and b) normalised simulated intensities from 2-spin density matrix simulations in SIMPSON. The pulses on $^{14}$N ($\nu_0$ = 36.1 MHz) were applied with a nutation frequency of 45 kHz for 9 μs. Recoupling was applied using either R$^3$, SPI-R$^3$, or SR4$_1^2$ (see Fig. 4), with their match conditions at $\nu_1 = 2\nu_r$ = 100 kHz, for a recoupling time of 10 rotor periods (200 μs).

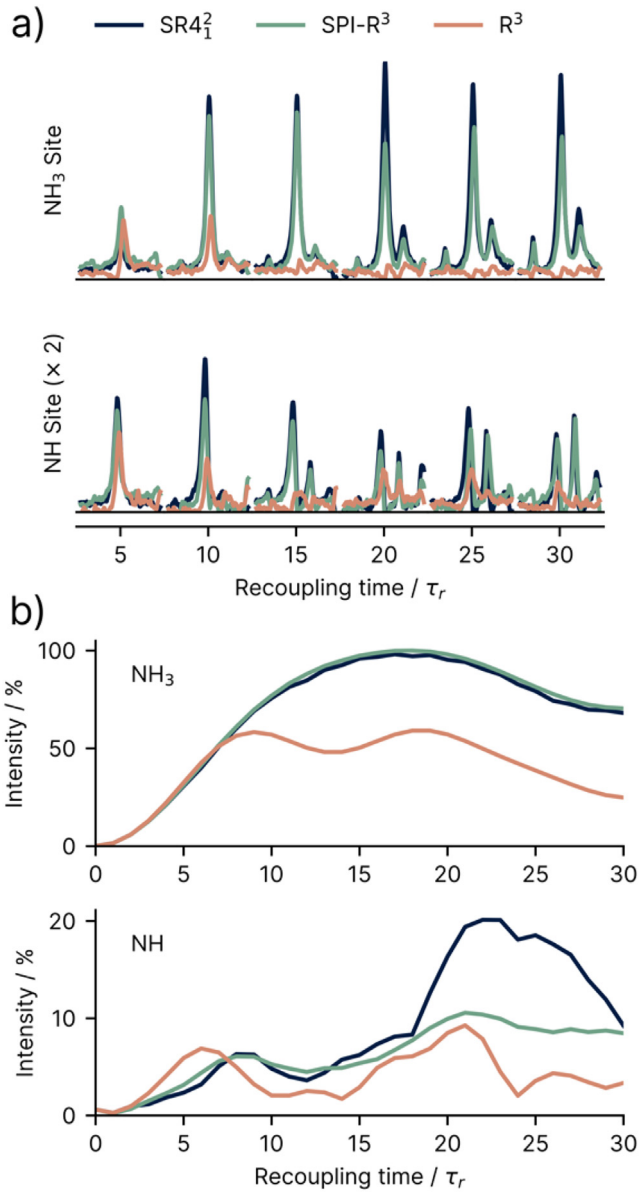


**Fig. 6.** Variation in $^{14}$N-$^1$H D-HMQC (see Fig. 1a) MAS NMR efficiency as function of the recoupling time for each of the three $^1$H-channel recoupling techniques considered here (see Fig. 4), as applied to β-AspAla at 50 kHz MAS and at a $^1$H Larmor frequency of 500 MHz. a) Experimental spectra extracted by summing rows of 2D spectra over the sites of interest and b) normalised simulated intensities from 2-spin density matrix simulations in SIMPSON. A nutation frequency of 100 kHz applied during the recoupling, corresponding to the $n$ = 2 condition for R$^3$. The pulses on $^{14}$N ($\nu_0$ = 36.1 MHz) were applied with a nutation frequency of 45 kHz for 9 μs.

most of the signal lost for both sites at a duration of 15 rotor periods. Both SPI-R$^3$ and SR4$_1^2$ show good efficiency at longer recoupling durations.

It should be noted that these recoupling schemes are all very sensitive to the pulses applied to the $^{14}$N channel for excitation and reconversion of the multiple quantum state, specifically exhibiting a marked dependence on the quadrupolar environments of the sites of interest. Considering these pulses in depth is beyond the scope of this article, and we would point an interested reader to the comprehensive study on these by Rankin et al, [59] where the authors evaluated a range of pulses including hard pulses, soft long pulses, DANTE pulse schemes, and phase inverted schemes.

### *3.4. $^{14}$N-$^1$H T-HMQC MAS NMR: Optimisation of TRAPDOR recoupling for β-aspartyl L-alanine using experiment and density matrix simulation and comparison with D-HMQC with SR4$_1^2$ recoupling at 60 kHz MAS*

Recently, the TRAnsfer of Population in DOuble Resonance (TRAPDOR) [27,29] approach has been applied in $^1$H-$^{14}$N heteronuclear correlation experiments for L-histidine. HCl·H$_2$O and *N*-acetyl-valine; TRAPDOR has been observed to offer greater efficiency than SR4$_1^2$ [7,30]. The pulse sequence for the T-HMQC experiment is shown in Fig. 1b. In this approach, RF is applied on the $^{14}$N channel. One benefit of TRAPDOR recoupling is that the nutation frequency applied during the recoupling interval is independent

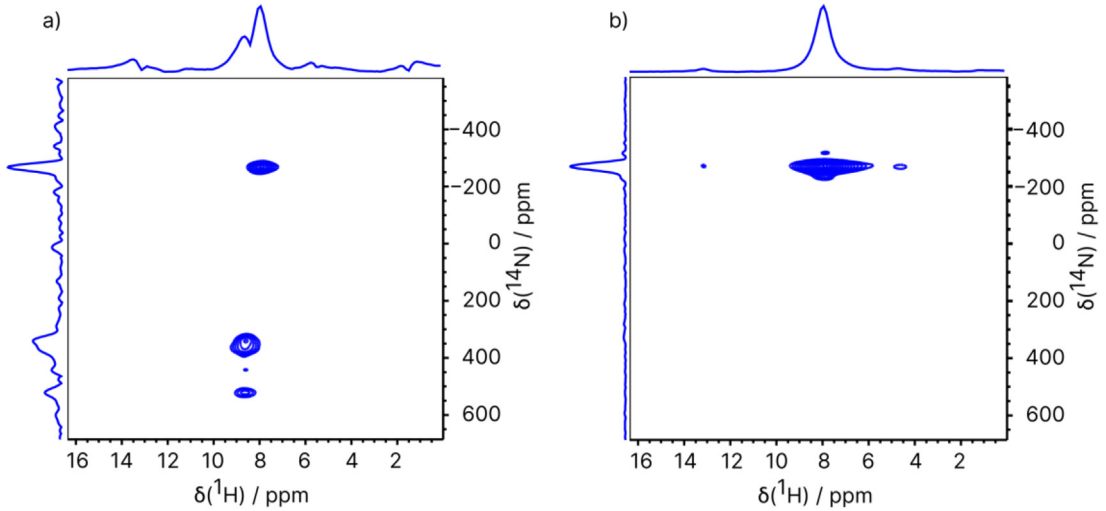


**Fig. 7.** 2D $^{14}$N-$^{1}$H ($^{1}$H $\nu_0$ = 500 MHz, $^{14}$N $\nu_0$ = 36.1 MHz) T-HMQC 60 kHz MAS NMR spectra with skyline projections of β-AspAla recorded with 40 $\tau_r$ (667 μs) of TRAPDOR recoupling at a $^{14}$N nutation frequency of 40 kHz. The $NH_3^+$ peak is at ∼−270 ppm, while the NH peak is ∼360 ppm. The transmitter was placed at (a) 75 kHz over the sideband of the NH peak and (b) at 55 kHz over the sideband of the $NH_3^+$ peak. Frequencies are stated relative to the $^{14}$N transmitter at −3 ppm. The base contour level is at (a) 22.4% and (b) 5.2% of the maximum peak intensity (noting that this corresponds to having the same intensity for the base contour in both spectra).

of the spinning frequency, as it relies on energy level crossings as opposed to rotary resonance- or symmetry-based recoupling [27]. However, these recoupling pulses applied on $^{14}$N have been observed to exhibit a significant dependence on their offset with respect to the sidebands of the peaks of interest [30]. This is of particular importance for observing compounds where there are multiple nitrogen environments with significantly different quadrupolar environments.

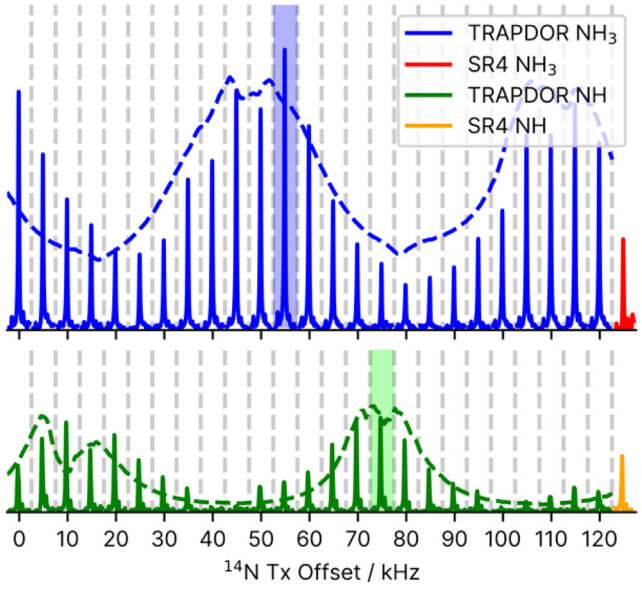


**Fig. 8.** Experimental spectra (solid lines, extracted by summing rows of 2D spectra over the sites of interest) and simulated (dashed lines) $^{14}$N-$^{1}$H T-HMQC MAS NMR intensity as a function of the $^{14}$N resonance offset for the $NH_3^+$ (blue) and NH (green) sites in β-AspAla recorded with 40 $\tau_r$ (667 μs) of TRAPDOR recoupling at a $^{14}$N nutation frequency of 40 kHz, a spinning frequency of 60 kHz and a $^{1}$H Larmor frequency of 500 MHz. Experimental spectra are also shown for the D-HMQC sequence with $SR4_1^2$ recoupling, using a $^{14}$N nutation frequency of 45 kHz for the $^{14}$N pulse lengths of 9 μs, which were optimized to give the best signal on the NH site. The offset conditions used in later figures are highlighted as the peak intensities for each site, at 55 kHz and 75 kHz respectively. Frequencies are stated relative to the $^{14}$N transmitter at −3 ppm. This separation of 20 kHz corresponds to 554 ppm. (For interpretation of the references to colour in this figure legend, the reader is referred to the web version of this article.)

Fig. 7 illustrates the challenge: as noted above, β-aspartyl alanine contains two nitrogen environments with significantly different quadrupolar environments (see Table 1 and Section 3.1). Owing

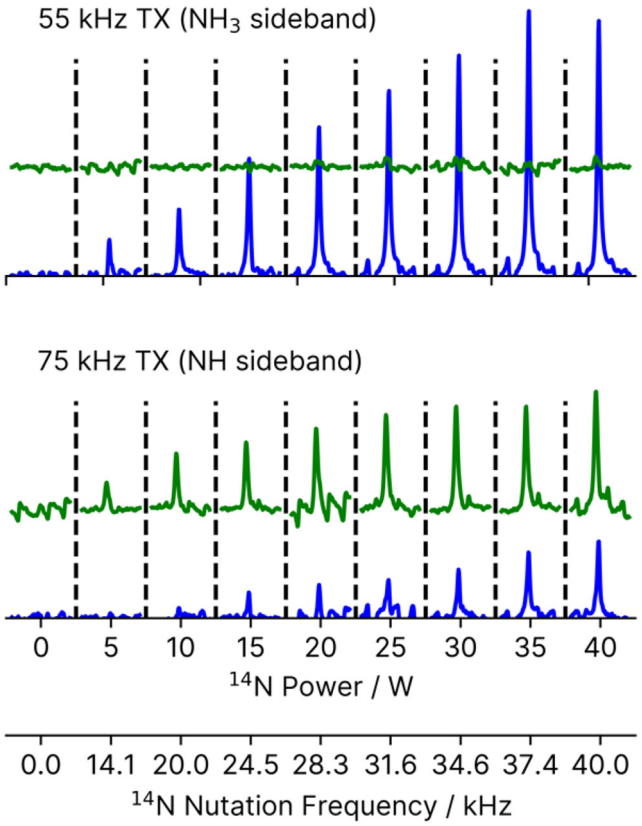


**Fig. 9.** Variation in the $^{14}$N-$^{1}$H T-HMQC MAS NMR intensity as a function of $^{14}$N nutation frequency with 40 $\tau_r$ (667 μs) of TRAPDOR recoupling (note: the power level was varied linearly, but the nutation frequency has a quadratic dependence on the power and so does not vary linearly). Experiments performed on β-AspAla, at a spinning frequency of 60 kHz and a $^{1}$H Larmor frequency of 500 MHz. The transmitter was set to be on a sideband of the $NH_3^+$ peak (top, $NH_3^+$ peak in blue) and on the sideband of the NH peak (bottom, NH peak in green). The 1D spectra were extracted by summing rows of 2D spectra over the sites of interest. (For interpretation of the references to colour in this figure legend, the reader is referred to the web version of this article.)

to the isotropic second-order quadrupolar chemical shift, this means that the two sites are separated by ~600 ppm at a $^{14}$N Larmor frequency of 36.12 MHz (see Fig. 3 above). Fig. 7a shows that, when the transmitter frequency is suitably chosen, it is possible to observe both the NH and $NH_3^+$ sites with reasonable efficiency, while Fig. 7b shows that it is possible to choose the transmitter frequency in such a way that optimum efficiency is obtained for the low-$C_Q$ $NH_3^+$ site, but the high-$C_Q$ NH site is not observed. This is further illustrated by Fig. 8, where both experiment and 2-spin simulations show that the transmitter offset corresponding to optimum efficiency is different for the NH and $NH_3^+$ sites. As such, the selection of the $^{14}$N offset of the TRAPDOR pulses is a compromise between the two sites. This is analogous to the sensitivity of the $^{14}$N excitation and reconversion pulse lengths in the D-HMQC experiment [59]. Note, however, that, in the case of TRAPDOR recoupling, it is the creation of the two spin $I_+S_z$ state which is affected, as opposed to the excitation of the multiple-quantum $I_+S_\pm$ state in the D-HMQC experiment [30].

Fig. 8 also presents a comparison of the T-HMQC and the D-HMQC experiments: Our observation of better sensitivity for the T-HMQC experiment is consistent with that observed by Hung et al for L-histidine·HCl·$H_2O$ [30] Fig. 9 shows the experimental dependence of the intensity in the T-HMQC experiment as the $^{14}$N nutation frequency applied during TRAPDOR recoupling is increased. With the transmitter over the $NH_3^+$ sideband (top), even with the highest $^{14}$N nutation frequency of 40 kHz, there is no evident signal apparent for the NH site. By comparison, as previously noted for Fig. 7b, it is possible to observe reasonable signal intensity for the low-$C_Q$ $NH_3^+$ site by using a higher $^{14}$N nutation frequency on the NH sideband.

## 4. Summary and outlook

This paper has considered two classes of $^{14}$N-$^1$H HMQC experiment for application under MAS, namely the D-HQMC experiment based on the $n$ = 2 rotary-resonance recoupling condition and the T-HMQC experiment using TRAPDOR. Our study has considered the case where there are $^{14}$N sites with a high and a low quadrupolar coupling constant, specifically for the dipeptide, β-AspAla. For the D-HMQC experiment, we find that $SR4_1^2$ and $SPI\text{-}R^3$ gave similar recoupling efficiency. While the T-HMQC TRAPDOR experiment gives enhanced sensitivity if optimised for one of the sites, it is observed to be sensitive to the choice of the $^{14}$N transmitter frequency, necessitating a compromise if a spectrum showing both $^{14}$N sites is to be recorded. This issue is exacerbated at lower magnetic fields, owing to the $B_0$ dependence of the second order quadrupolar isotropic shift. However, the potential for TRAPDOR to act as a site specific filter may be of interest for the development of experiments in which selection of a specific nitrogen environment is required, for example in the use of selective SOFAST-type HMQC experiments [60] or for isolation of specific $^1$H environments to probe $^{14}$N-$^1$H proximities [61].

## Data availability

Link given in Acknowledgements to the data set.

## Declaration of Competing Interest

The authors declare that they have no known competing financial interests or personal relationships that could have appeared to influence the work reported in this paper.

## Acknowledgements

BT thanks Bruker and the University of Warwick for PhD funding as part of the Warwick Centre for Doctoral Training in Analytical Science. Computing facilities were provided by the Scientific Computing Research Technology Platform of the University of Warwick. This project benefitted from interaction with the EPSRC-funded (EP/T026642/1) Collaborative Computational Project for NMR Crystallography, CCP-NC. We thank Dr Andrew P. Howes and Patrick Ruddy for supporting the operation of the Millburn House Magnetic Resonance Laboratory. Data for this study are provided as a supporting data set from the University of Warwick Research Datasets portal at https://wrap.warwick.ac.uk/175450/.

## Appendix A. Supplementary material

Supplementary data to this article can be found online at https://doi.org/10.1016/j.jmr.2023.107459.

## References

[1] S. Cavadini, S. Antonijevic, A. Lupulescu, G. Bodenhausen, Indirect detection of nitrogen-14 in solid-state NMR spectroscopy, ChemPhysChem 8 (2007) 1363–1374, https://doi.org/10.1002/cphc.200700049.
[2] Z. Gan, Measuring amide nitrogen quadrupolar coupling by high-resolution $^{14}$N/$^{13}$C NMR correlation under magic-angle spinning, J. Am. Chem. Soc. 128 (2006) 6040–6041, https://doi.org/10.1021/ja0578597.
[3] Z. Gan, J.P. Amoureux, J. Trébosc, Proton-detected $^{14}$N MAS NMR using homonuclear decoupled rotary resonance, Chem. Phys. Lett. 435 (2007) 163–169, https://doi.org/10.1016/j.cplett.2006.12.066.
[4] Y. Nishiyama, Y. Endo, T. Nemoto, H. Utsumi, K. Yamauchi, K. Hioka, T. Asakura, Very fast magic angle spinning $^1$H–$^{14}$N 2D solid-state NMR: Sub-micro-liter sample data collection in a few minutes, J. Magn. Reson. 208 (2011) 44–48, https://doi.org/10.1016/j.jmr.2010.10.001.
[5] A.L. Webber, S. Masiero, S. Pieraccini, J.C. Burley, A.S. Tatton, D. Iuga, T.N. Pham, G.P. Spada, S.P. Brown, Identifying Guanosine Self Assembly at Natural Isotopic Abundance by High-Resolution $^1$H and $^{13}$C Solid-State NMR Spectroscopy, J. Am. Chem. Soc. 133 (2011) 19777–19795, https://doi.org/10.1021/ja206516u.
[6] A.S. Tatton, T.N. Pham, F.G. Vogt, D. Iuga, A.J. Edwards, S.P. Brown, Probing intermolecular interactions and nitrogen protonation in pharmaceuticals by novel $^{15}$N-edited and 2D $^{14}$N–$^1$H solid-state NMR, CrstEngComm 14 (2012) 2654–2659, https://doi.org/10.1039/c2ce06547a.
[7] J.A. Jarvis, M. Concistre, I.M. Haies, R.W. Bounds, I. Kuprov, M. Carravetta, P.T.F. F. Williamson, Quantitative analysis of $^{14}$N quadrupolar coupling using $^1$H detected $^{14}$N solid-state NMR, Phys. Chem. Chem. Phys. 21 (2019) 5941–5949, https://doi.org/10.1039/c8cp06276e.
[8] E.K. Corlett, H. Blade, L.P. Hughes, P.J. Sidebottom, D. Walker, R.I. Walton, S.P. Brown, An XRD and NMR crystallographic investigation of the structure of 2,6-lutidinium hydrogen fumarate, CrstEngComm 21 (2019) 3502–3516, https://doi.org/10.1039/c9ce00633h.
[9] E.K. Corlett, H. Blade, L.P. Hughes, P.J. Sidebottom, D. Walker, R.I. Walton, S.P. Brown, 5-amino-2-methylpyridinium hydrogen fumarate: An XRD and NMR crystallography analysis, Magn. Reson. Chem. 58 (2020) 1026–1035, https://doi.org/10.1002/mrc.5021.
[10] K. Bártová, I. Císařová, A. Lyčka, M. Dračínský, Tautomerism of azo dyes in the solid state studied by $^{15}$N, $^{14}$N, $^{13}$C and $^1$H NMR spectroscopy, X-ray diffraction and quantum-chemical calculations, Dyes Pigm. 178 (2020) 108342, https://doi.org/10.1016/j.dyepig.2020.108342.
[11] M. Grüne, R. Luxenhofer, D. Iuga, S.P. Brown, A.C. Pöppler, $^{14}$N–$^1$H HMQC solid-state NMR as a powerful tool to study amorphous formulations-an exemplary study of paclitaxel loaded polymer micelles, J. Mater. Chem. B. 8 (2020) 6827–6836, https://doi.org/10.1039/d0tb00614a.
[12] A. Pugliese, M. Toresco, D. Mcnamara, D. Iuga, A. Abraham, M. Tobyn, L.E. Hawarden, F. Blanc, Drug-Polymer Interactions in Acetaminophen/Hydroxypropylmethylcellulose Acetyl Succinate Amorphous Solid Dispersions Revealed by Multidimensional Multinuclear Solid-State NMR Spectroscopy, Mol. Pharm. 18 (2021) 3519–3531, https://doi.org/10.1021/acs.molpharmaceut.1c00427.
[13] D. Bernasconi, S. Bordignon, F. Rossi, E. Priola, C. Nervi, R. Gobetto, D. Voinovich, D. Hasa, N.T. Duong, Y. Nishiyama, M.R. Chierotti, Selective Synthesis of a Salt and a Cocrystal of the Ethionamide-Salicylic Acid System, Cryst. Growth Des. 20 (2020) 906–915, https://doi.org/10.1021/acs.cgd.9b01299.
[14] A.S. Tatton, J.P. Bradley, D. Iuga, S.P. Brown, $^{14}$N–$^1$H heteronuclear multiple-quantum correlation magic-angle spinning NMR spectroscopy of organic solids, Z. Phys. Chemie 226 (2012) 1187–1203, https://doi.org/10.1524/zpch.2012.0308.
[15] A.S. Tatton, T.N. Pham, F.G. Vogt, D. Iuga, A.J. Edwards, S.P. Brown, Probing hydrogen bonding in cocrystals and amorphous dispersions using $^{14}$N–$^1$H

HMQC solid-state NMR, Mol. Pharm. 10 (2013) 999–1007, https://doi.org/10.1021/mp300423r.
[16] M.K. Pandey, J.-P. Amoureux, T. Asakura, Y. Nishiyama, Sensitivity enhanced $^{14}N/^{14}N$ correlations to probe inter-beta-sheet interactions using fast magic angle spinning solid-state NMR in biological solids, Phys. Chem. Chem. Phys. 18 (2016), https://doi.org/10.1039/c6cp03848d.
[17] M.K. Pandey, J.T. Damron, A. Ramamoorthy, Y. Nishiyama, Proton-detected 3D $^{1}H$ anisotropic/$^{14}N/^{1}H$ isotropic chemical shifts correlation NMR under fast magic angle spinning on solid samples without isotopic enrichment, Solid State Nucl. Magn. Reson. 97 (2019) 40–45, https://doi.org/10.1016/j.ssnmr.2018.12.002.
[18] T. Venâncio, L.M. Oliveira, J. Ellena, N. Boechat, S.P. Brown, Probing intermolecular interactions in a diethylcarbamazine citrate salt by fast MAS $^{1}H$ solid-state NMR spectroscopy and GIPAW calculations, Solid State Nucl. Magn. Reson. 87 (2017) 73–79, https://doi.org/10.1016/j.ssnmr.2017.02.006.
[19] D. Carnevale, X. Ji, G. Bodenhausen, Double cross polarization for the indirect detection of nitrogen-14 nuclei in magic angle spinning NMR spectroscopy, J. Chem. Phys. 147 (2017) 184201, https://doi.org/10.1063/1.5000689.
[20] D. Carnevale, B. Grosjean, G. Bodenhausen, Dipolar couplings in solid polypeptides probed by $^{14}N$ NMR spectroscopy, Commun. Chem. 1 (2018) 73, https://doi.org/10.1038/s42004-018-0072-5.
[21] Y. Hong, T. Asakura, Y. Nishiyama, 3D $^{14}N/^{1}H$ Double Quantum/$^{1}H$ Single Quantum Correlation Solid-State NMR for Probing the Parallel and Anti-Parallel Beta-Sheet Arrangement of Oligo-Peptides at Natural Abundance, ChemPhysChem 19 (2018) 1841–1845, https://doi.org/10.1002/cphc.201800392.
[22] D.P. Raleigh, M.H. Levitt, R.G. Griffin, Rotational resonance in solid state NMR, Chem. Phys. Lett. 146 (1988) 71–76, https://doi.org/10.1016/0009-2614(88)85051-6.
[23] M.H. Levitt, Symmetry-Based Pulse Sequences in Magic-Angle Spinning Solid-State NMR, in: Encycl. Nucl. Magn. Reson., John Wiley & Sons Ltd, Chichester, 2002, pp. 165–196.
[24] S.-J. Huang, S.-B. Liu, J.C.C. Chan, Heteronuclear dipolar recoupling of half-integer quadrupole nuclei under fast magic angle spinning, Solid State Nucl. Magn. Reson. 36 (2009) 110–117, https://doi.org/10.1016/j.ssnmr.2009.07.002.
[25] P.R. Costa, J.D. Gross, M. Hong, R.G. Griffin, Solid-state NMR measurement of Ψ in peptides: a NCCN 2Q-heteronuclear local field experiment, Chem. Phys. Lett. 280 (1997) 95–103, https://doi.org/10.1016/S0009-2614(97)01107-X.
[26] A. Brinkmann, A.P.M.M. Kentgens, Proton-selective $^{17}O–^{1}H$ distance measurements in fast magic-angle-spinning solid-state NMR spectroscopy for the determination of hydrogen bond lengths, J. Am. Chem. Soc. 128 (2006) 14758–14759, https://doi.org/10.1021/ja065415k.
[27] C.P. Grey, A.J. Vega, Determination of the Quadrupole Coupling Constant of the Invisible Aluminum Spins in Zeolite HY with $^{1}H/^{27}Al$ TRAPDOR NMR, J. Am. Chem. Soc. 117 (1995) 8232–8242, https://doi.org/10.1021/ja00136a022.
[28] T. Gullion, Measurement of dipolar interactions between spin-1/2 and quadrupolar nuclei by rotational-echo, adiabatic-passage, double-resonance NMR, Chem. Phys. Lett. 246 (1995) 325–330, https://doi.org/10.1016/0009-2614(95)01120-x.
[29] Q. Zeng, H. Nekvasil, C.P. Grey, Proton Environments in Hydrous Aluminosilicate Glasses: A $^{1}H$ MAS, $^{1}H/^{27}Al$, and $^{1}H/^{23}Na$ TRAPDOR NMR Study, J. Phys. Chem. B. 103 (1999) 7406–7415, https://doi.org/10.1021/jp990726l.
[30] I. Hung, P. Gor'kov, Z. Gan, P. Gor'kov, Z. Gan, Efficient and sideband-free $^{1}H$-detected $^{14}N$ magic-angle spinning NMR, J. Chem. Phys. 151 (2019), https://doi.org/10.1063/1.5126599.
[31] I. Hung, Z. Gan, High-resolution NMR of S = 3/2 quadrupole nuclei by detection of double-quantum satellite transitions via protons, J. Phys. Chem. Lett. 11 (2020) 4734–4740, https://doi.org/10.1021/acs.jpclett.0c01236.
[32] R. Bayzou, J. Trébosc, I. Hung, Z. Gan, O. Lafon, J.-P. Amoureux, Indirect NMR detection via proton of nuclei subject to large anisotropic interactions, such as $^{14}N$, $^{195}Pt$, and $^{35}Cl$, using the T-HMQC sequence, J. Chem. Phys. 156 (2022) 064202, https://doi.org/10.1063/5.0082700.
[33] U. Sternberg, R. Witter, I. Kuprov, J.M. Lamley, A. Oss, J.R. Lewandowski, A. Samoson, $^{1}H$ line width dependence on MAS speed in solid state NMR - comparison of experiment and simulation, J. Magn. Reson. 291 (2018) 32–39, https://doi.org/10.1016/j.jmr.2018.04.003.
[34] S. Hayashi, K. Hayamizu, Chemical shift standards in high-resolution solid-state NMR (2) $^{15}N$ Nuclei, Bull. Chem. Soc. Jpn. 64 (1991) 688–690, https://doi.org/10.1246/bcsj.64.688.
[35] R.K. Harris, E.D. Becker, S.M. Cabral De Menezes, P. Granger, R.E. Hoffman, K.W. Zilm, Further conventions for NMR shielding and chemical shifts (IUPAC Recommendations 2008), Pure Appl. Chem. 80 (2008) 59–84, https://doi.org/10.1351/pac200880010059.
[36] G.E. Martin, C.E. Hadden, Long-range $^{1}H–^{15}N$ heteronuclear shift correlation at natural abundance, J. Nat. Prod. 63 (2000) 543–585, https://doi.org/10.1021/np9903191.
[37] M.D. Segall, P.J.D. Lindan, M.J. Probert, C.J. Pickard, P.J. Hasnip, S.J. Clark, M.C. Payne, First-principles simulation: ideas, illustrations and the CASTEP code, J. Phys. Condens. Matter. 14 (2002) 2717, https://doi.org/10.1088/0953-8984/14/11/301.
[38] C.H. Görbitz, P. Strande, K. Undheim, R.W. Taft, G.W. Fischer, Crystal and molecular structures of the isomeric dipeptides alpha-L-Aspartyl-L-alanine and beta-L-Aspartyl-L-alanine, Acta Chem. Scand. 41b (1987) 679–685, https://doi.org/10.3891/acta.chem.scand.41b-0679.
[39] J.P. Perdew, K. Burke, M. Ernzerhof, Generalized gradient approximation made simple, Phys. Rev. Lett. 77 (1996) 3865–3868, https://doi.org/10.1103/PhysRevLett.77.3865.
[40] C.J. Pickard, F. Mauri, All-electron magnetic response with pseudopotentials: NMR chemical shifts, Phys. Rev. B. 63 (2001) 245101, https://doi.org/10.1103/physrevb.63.245101.
[41] J.R. Yates, C.J. Pickard, F. Mauri, Calculation of NMR chemical shifts for extended systems using ultrasoft pseudopotentials, Phys. Rev. B. 76 (2007) 24401, https://doi.org/10.1103/physrevb.76.024401.
[42] M. Bak, J.T. Rasmussen, N.C. Nielsen, SIMPSON: A General Simulation Program for Solid-State NMR Spectroscopy, J. Magn. Reson. 147 (2000) 296–330, https://doi.org/10.1006/jmre.2000.2179.
[43] Z. Tošner, R. Andersen, B. Stevensson, M. Edén, N.C. Nielsen, T. Vosegaard, Computer-intensive simulation of solid-state NMR experiments using SIMPSON, J. Magn. Reson. 246 (2014) 79–93, https://doi.org/10.1016/j.jmr.2014.07.002.
[44] Z. Tošner, T. Vosegaard, C. Kehlet, N. Khaneja, S.J. Glaser, N.C. Nielsen, Optimal control in NMR spectroscopy: Numerical implementation in SIMPSON, J. Magn. Reson. 197 (2009) 120–134, https://doi.org/10.1016/j.jmr.2008.11.020.
[45] M. Bak, N.C. Nielsen, REPULSION, A novel approach to efficient powder averaging in solid-state NMR, J. Magn. Reson. 125 (1997) 132–139, https://doi.org/10.1006/jmre.1996.1087.
[46] S. Sturniolo, T.F.G. Green, R.M. Hanson, M. Zilka, K. Refson, P. Hodgkinson, S.P. Brown, J.R. Yates, Visualization and processing of computed solid-state NMR parameters: MagresView and MagresPython, Solid State Nucl. Magn. Reson. 78 (2016) 64–70, https://doi.org/10.1016/j.ssnmr.2016.05.004.
[47] K. Xue, R. Sarkar, C. Motz, S. Asami, V. Decker, S. Wegner, Z. Tosner, B. Reif, Magic-angle spinning frequencies beyond 300 kHz are necessary to yield maximum sensitivity in selectively methyl protonated protein samples in solid-state NMR, J. Phys. Chem. C. 122 (2018) 16437–16442, https://doi.org/10.1021/acs.jpcc.8b05600.
[48] A. Samoson, E. Lippmaa, A. Pines, High resolution solid-state N.M.R. Averaging of second-order effects by means of a double-rotor, Mol. Phys. 65 (1988) 1013–1018, https://doi.org/10.1080/00268978800101571.
[49] S.P. Brown, A. Lesage, B. Elena, L. Emsley, Probing proton–proton proximities in the solid state: high-resolution two-dimensional $^{1}H–^{1}H$ double-quantum CRAMPS NMR spectroscopy, J. Am. Chem. Soc. 126 (2004) 13230–13231, https://doi.org/10.1021/ja045461p.
[50] S. Dusold, A. Sebald, Dipolar recoupling under magic-angle spinning conditions, in: Annu. Reports NMR Spectrosc., Academic Press, 2000, pp. 185–264, https://doi.org/10.1016/s0066-4103(00)41010-0.
[51] T.G. Oas, R.G. Griffin, M.H. Levitt, Rotary resonance recoupling of dipolar interactions in solid-state nuclear magnetic resonance spectroscopy, J. Chem. Phys. 89 (1988) 692–695, https://doi.org/10.1063/1.455191.
[52] X. Lu, O. Lafon, J. Trébosc, G. Tricot, L. Delevoye, F. Méar, L. Montagne, J.P. Amoureux, Observation of proximities between spin-1/2 and quadrupolar nuclei: Which heteronuclear dipolar recoupling method is preferable?, J Chem. Phys. 137 (2012), https://doi.org/10.1063/1.4753987.
[53] M. Ernst, A. Samoson, B.H. Meier, Decoupling and recoupling using continuous-wave irradiation in magic-angle-spinning solid-state NMR: A unified description using bimodal Floquet theory, J. Chem. Phys. 123 (2005) 64102, https://doi.org/10.1063/1.1944291.
[54] S. Cavadini, A. Abraham, G. Bodenhausen, Proton-detected nitrogen-14 NMR by recoupling of heteronuclear dipolar interactions using symmetry-based sequences, Chem. Phys. Lett. 445 (2007) 1–5, https://doi.org/10.1016/j.cplett.2007.07.060.
[55] A.S. Tatton, H. Blade, S.P. Brown, P. Hodgkinson, L.P. Hughes, S.O.N. Lill, J.R. Yates, Improving confidence in crystal structure solutions using NMR crystallography: The case of β-Piroxicam, Cryst. Growth Des. 18 (2018) 3339–3351, https://doi.org/10.1021/acs.cgd.8b00022.
[56] N.T. Duong, F. Rossi, M. Makrinich, A. Goldbourt, M.R. Chierotti, R. Gobetto, Y. Nishiyama, Accurate $^{1}H–^{14}N$ distance measurements by phase-modulated RESPDOR at ultra-fast MAS, J. Magn. Reson. 308 (2019) 106559, https://doi.org/10.1016/j.jmr.2019.07.046.
[57] K. Aebischer, Z. Tošner, M. Ernst, Effects of radial radio-frequency field inhomogeneity on MAS solid-state NMR experiments, Magn. Reson. 2 (2021) 523–543, https://doi.org/10.5194/mr-2-523-2021.
[58] K. Maruyoshi, D. Iuga, O.N. Antzutkin, A. Alhalaweh, S.P. Velaga, S.P. Brown, Identifying the intermolecular hydrogen-bonding supramolecular synthons in an indomethacin–nicotinamide cocrystal by solid-state NMR, Chem. Commun. 48 (2012) 10844–10846, https://doi.org/10.1039/c2cc36094b.
[59] A.G.M.M. Rankin, J. Trébosc, P. Paluch, O. Lafon, J.P. Amoureux, Evaluation of excitation schemes for indirect detection of $^{14}N$ via solid-state HMQC NMR experiments, J. Magn. Reson. 303 (2019) 28–41, https://doi.org/10.1016/j.jmr.2019.04.004.
[60] A.V. Wijesekara, A. Venkatesh, B.J. Lampkin, B. VanVeller, J.W. Lubach, K. Nagapudi, I. Hung, P.L. Gor'kov, Z. Gan, A.J. Rossini, P.L. Gor'kov, Z. Gan, A.J. Rossini, Fast acquisition of proton-detected HETCOR solid-state NMR spectra of quadrupolar nuclei and rapid measurement of NH bond lengths by frequency selective HMQC and RESPDOR pulse sequences, Chem. - A Eur. J. 26 (2020) 7881–7888, https://doi.org/10.1002/chem.202000390.
[61] Y. Ogaeri, N. Suzuki, T. Fukami, Y. Nishiyama, Internuclear distance measurements between $^{1}H$ and $^{14}N$ in multi-component rigid solids at fast MAS, J. Magn. Reson. 348 (2023), https://doi.org/10.1016/j.jmr.2023.107378.